


## Microwave Spin-Torque-Induced Magnetic Resonance in a Nanoring-Shape-Confined Magnetic Tunnel Junction

Jianying Qin,<sup>1</sup> Xing Chen,<sup>2</sup> Tian Yu,<sup>3</sup> Xiao Wang,<sup>1</sup> Chenyang Guo,<sup>1</sup> Caihua Wan,<sup>1</sup> Jiafeng Feng,<sup>1</sup> Hongxiang Wei,<sup>1</sup> Yaowen Liu,<sup>2,\*</sup> and Xiufeng Han<sup>1,†</sup>

<sup>1</sup>*Beijing National Laboratory for Condensed Matter Physics, Institute of Physics, Chinese Academy of Sciences, University of Chinese Academy of Sciences, Beijing 100190, China*

<sup>2</sup>*School of Physics Science and Engineering, Tongji University, Shanghai 200092, China*

<sup>3</sup>*College of Physical Science and Technology, Sichuan University, Chengdu 610065, China*

 (Received 1 June 2018; revised manuscript received 20 August 2018; published 29 October 2018)

The characters of spin torque ferromagnetic resonance (ST FMR) are systematically studied in the nanoscale ring-shape confined magnetic tunnel junctions (MTJs). Different from the continuous magnetic films, the confined structure shows two resonance states with different resonance frequencies at a given external magnetic field. The two resonance states both originate from the free layer (FL) of MTJs and their resonance frequencies show a blueshift behavior with an increase of the magnetic field. The two states have been recognized by micromagnetic simulations and supported by theoretical analysis as the acoustic-like and optical-like fundamental resonance modes, respectively. They correspond to the in-phase and antiphase localized magnetization oscillation within the FL itself. In addition to the fundamental modes, high-order harmonic signals are also theoretically predicted. This study provides deep understanding of ferromagnetic resonance states in the geometrically confined MTJ structures, which may be applicable to develop spin-torque-based dual-mode microwave detectors.

DOI: [10.1103/PhysRevApplied.10.044067](https://doi.org/10.1103/PhysRevApplied.10.044067)

### I. INTRODUCTION

Seeking spintronics devices with high-performance and low-energy consumption [1,2], for example, spin-transfer torque-based magnetic random access memory (STT MRAM) [3–6], inevitably requires minimizing the element cell size, by which the critical switching current can be reduced and the areal density of the memory can be improved. However, the reduction of the element size in turn produces an obvious confinement effect [7,8], which inversely leads to some quite different magnetization configurations and dynamic properties compared with conventional macroscale devices. Therefore, investigation of magnetization states and magnetic dynamics in the nanosize-confined magnetic structures is crucial for both fundamental physics and practical applications.

The spin-torque ferromagnetic resonance (ST FMR) technique is one of the most convenient methods that can provide rich information about magnetic dynamics in different kinds of magnetic systems [6,9–12]. In the last few years, various magnetic dynamic properties, such as effective damping constant and spin-transfer torquances, have been investigated by ST FMR in nanosized magnetic

tunnel junctions (MTJs). It has been found that the resonance field ( $H_{\text{res}}$ ) can be shifted in comparison with the continuous films. There are several mechanisms that are related to the shift of  $H_{\text{res}}$ : magnetization homogeneity [6,13], demagnetizing field [14], exchange coupling between the free layer (FL) and reference layer (RL) [15]. Moreover, the geometric confinement effect in such nanosized MTJs may also play an important role in controlling magnetic dynamics properties [16–18], but it has not been well understood until now. As one of the most appropriate geometrically confined nanoscale devices, the nanoring-shaped MTJs (NR MTJs) are noteworthy candidates. First, since the ring shape can provide a closure magnetic flux, the magnetic configuration, therefore, can be easily controlled between vortex and onion states [19–21]. Second, the magnetization dynamics of NR MTJs can be directly controlled by spin-polarized current through the spin-transfer torque effect (STT) effect [22–24], and can be affected by the current-induced in-plane circular Oersted field [21].

In this study, the confinement effect on magnetization precession in the FL itself of NR MTJs is investigated by ST FMR measurement together with micromagnetic simulation in both time and frequency domains. Two different fundamental resonance modes are experimentally observed in ST FMR spectra under a given external

\*yaowen@tongji.edu.cn

†xfhan@iphy.ac.cn

magnetic field, which can be well reproduced by micro-magnetic simulations. In conventional FMR experiments in the coupled thin films, the bilayer exhibits two resonance states: an acoustic mode with the magnetizations in the two layers precessing in-phase and an optic mode with the magnetizations precessing antiphase [25–28]. But here we observe the two fundamental resonances originating from the same FL of the NR MTJs, forming the acoustic-like in-phase precession mode (mode 1) and the optic-like antiphase precession mode (mode 2), respectively. These two modes can be well described theoretically by the exchange-interaction-dominated standing-spin-wave model in a geometrically confined structure. In addition to the two fundamental resonance modes, higher-order harmonic resonances can also be excited, which is believed to be a joint effect of the propagation of nonuniform magnetization alteration and the NR-confined periodic boundary condition in NR MTJs. This result suggests the NR MTJs can be good candidates as microwave detectors with double detecting modes—two different frequencies at the resonance states (mode 1 and mode 2) can be activated and detected. This is more advantageous than the conventional ones, in which only one microwave mode can be detected under a given external field [29–31]. Furthermore, the high-order harmonic resonance states of these fundamental ones may further improve the sensitivity of the detector, which needs to be experimentally confirmed in future.

## II. EXPERIMENTAL METHOD

MgO-based in-plane MTJs film with the stack structure of a seed layer/PtMn(20)/CoFe(2.5)/Ru(0.8)/CoFeB(3)/MgO(1.3)/CoFeB(2)/cap layer (unit in nm) is deposited on Si/SiO<sub>2</sub> (300 nm) substrate, as shown in Fig. 1(a). The film is annealed at 400°C for 1 h before fabrication. NR MTJs with outer and inner diameters of  $(2R_1, 2R_2) = (120, 80)$  in nanometers are fabricated on a coplanar wave guide (CPW) by electron-beam lithography, photolithography, and Ar-ion milling processes. The top FL and bottom RL are connected to the signal line (S) and ground line (G) of the CPW, respectively. The SEM picture also shows the good quality of the NR MTJ. Figure 1(b) shows the homodyne-detection ST FMR setup. A microwave (MW) modulated by a low-frequency pulse ( $< 300$  Hz) is generated from a vector network analyzer (VNA) and injected into the NR MTJs. The resulting ST FMR signal, the mixing voltage ( $V_{\text{mix}}$ ), is then extracted by the lock-in amplifier (LiA). The ST FMR measurements are conducted at room temperature in the frequency domain (0.5–18 GHz). During the measurements, a constant in-plane magnetic field ( $H_{\parallel}$ ) with its direction deviating from the RL pinning direction ( $+x$ ) by  $12^\circ$  is applied, and by systematically changing  $H_{\parallel}$  from  $\pm 0.6$  kOe to  $\pm 3$  kOe, a series of ST FMR spectra are successfully obtained.

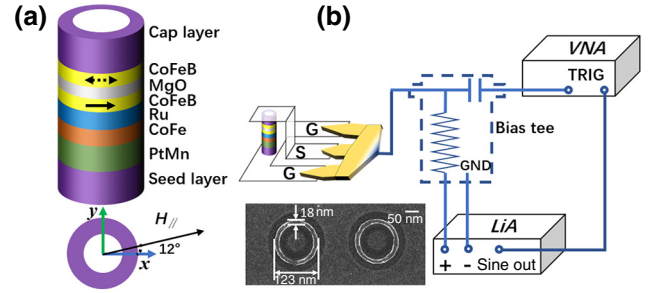


FIG. 1. (a) The MTJ layer structure and (b) The ST FMR measurement setup. The inset of (b) shows the SEM image of the NR MTJ.

## III. RESULTS AND DISCUSSION

Figure 2 shows a typical magnetization loop ( $M$ - $H$ ) and a magnetoresistance loop ( $R$ - $H$ ) ( $H$  long  $\pm x$  direction), in which the synthetic antiferromagnetic (SAF) layer in the structure of PtMn(20)/CoFe(2.5)/Ru(0.8)/CoFeB(3) switches as a single ferromagnetic layer with a large uniaxial anisotropy. Since the SAF-pinned bottom RL is well fixed unless  $H$  is higher than 3 kOe and the FL only has a low coercivity field of less than 0.5 kOe, the switching of the RL and FL can thus be well separated. The typical magnetoresistance ratio (MR) is about 104% at room temperature, indicating the high performance of the NR MTJs. A severe shift of the  $R$ - $H$  minor loop against  $H$  is observed in Fig. 2(b), which can be attributed to the effect of the stray field ( $H_{\text{str}}$ ) that is often observed in a SAF structure, due to the difficulty of completely compensating the magnetization.

In the following, the ST FMR spectra under a series of  $H_{\parallel}$  are summarized in Fig. 3(a). As shown, for both positive and negative  $H_{\parallel}$ , the resonant peaks gradually blueshift with increasing  $H_{\parallel}$  magnitude, which is consistent with the expectation derived from the Kittel formula [32,33]. However, also notice that the resonance peaks under negative  $H_{\parallel}$  always appear at the lower frequency side compared with that measured in the same amplitude of the positive field. This asymmetry can be attributed to the stray field ( $\sim 100$  Oe, along the  $+x$  direction), which will enhance (decrease) the total effective field ( $H_{\text{eff}}$ ) for the positive (negative)  $H_{\parallel}$  as  $H_{\text{eff}} = H_{\text{str}} \pm H_{\parallel}$ . Therefore, when the negative  $H_{\parallel}$  is applied, the  $H_{\text{eff}}$  sensed by FL is always lower than that when the positive  $H_{\parallel}$  is applied, resulting in a redshift of the resonant peaks at the negative  $H_{\parallel}$ . This has also been confirmed by the micromagnetic simulation in S-I within the Supplemental Material [34].

By fitting the spectra using a linear combination of Lorentzian  $L(f) = 1/[1 + (f - f_r)^2/\Delta_0^2]$  and anti-Lorentzian  $A(f) = [(f - f_r)/\Delta_0]L(f)$  as

$$V_{\text{mix}}(f) = C_s \times L(f) + C_a \times A(f) \quad (1)$$

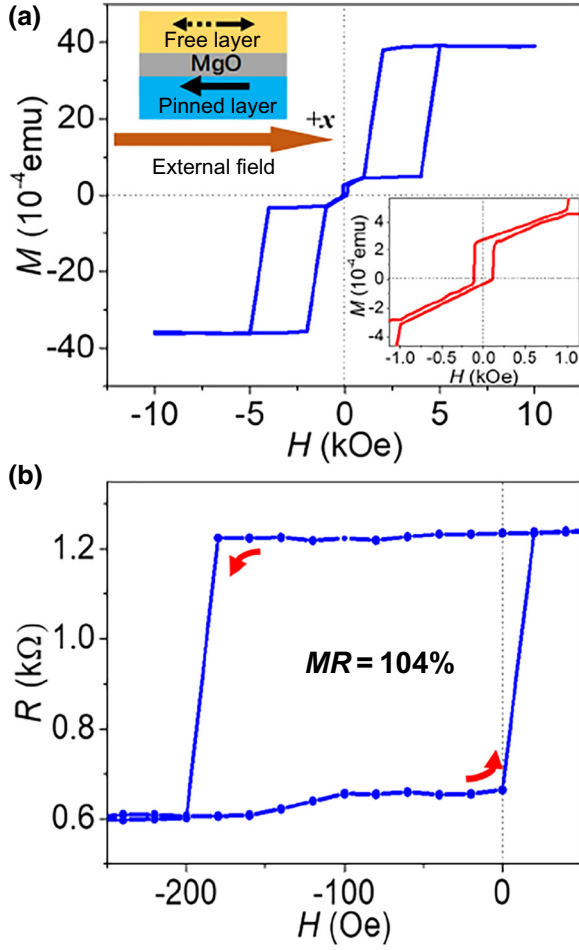


FIG. 2. (a) Magnetic hysteresis loop (M-H) with the magnetic field applied in-plane along the pinning direction, (b) The minor magnetoresistance loop (R-H) corresponding to the minor M-H loop shown the insert of (a).

we can obtain  $\Delta_0$  (spectra linewidth),  $C_s$  (intensity of symmetric component) and  $C_a$  (intensity of asymmetric component) [6]. Another noteworthy feature in the ST FMR spectra is that, at a given  $H_{\parallel}$ , it exhibits two resonance peaks with different frequencies ( $f_{r1}$  and  $f_{r2}$ ), as shown in Figs. 3(a) and 3(b). This two-peak property also exists in the series of NR MTJs with different size parameters as  $(2R_1, 2R_2) = \{(80,40), (100,60), (120,80), (150,75)\}$  in nanometers in our experiments (not shown here), which means that this two-peak property is typical in our NR MTJs. In the framework of macrospin approximation, where the magnetization of a nanomagnet is assumed to be uniform and the magnetization precession is treated coherently, it is known that only one resonant solution can usually be obtained by solving the Kittel equation at each magnetic field [35–39]. ST FMR spectra with multi-peaks have been reported in previous reports [40–44], in which the extra peaks are usually considered to result from the excitation of the RL resonance. However, in the results shown in Fig. 2(a), the RL of the NR MTJs is firmly pinned

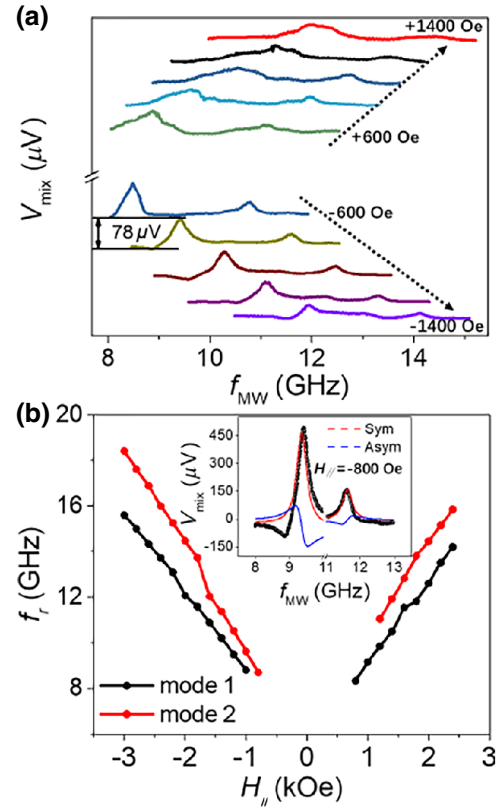


FIG. 3. (a) Typical ST FMR spectra measured from  $\pm 600$  Oe to  $\pm 1400$  Oe, where two resonant peaks are clearly observed. (b) Summary of resonance frequency as a function of the applied field. The inset of (b) shows an example of resonance peak fitting.

by the SAF structure when the amplitude of the magnetic field is between 600 and 3000 Oe. Therefore, the resonance in RL can be excluded and the observed two peaks can only originate from the FL. Moreover, it is noticed that  $f_{r1}$  and  $f_{r2}$  are not harmonically related, implying that the two resonance peaks correspond to two distinct resonance modes.

To gain insight into these spin-torque-driven resonance modes, micromagnetic simulations are performed using the open source simulation software OOMMF [45], which is based on the Landau-Lifshitz-Gilbert (LLG) equation, including two spin-torque terms:

$$\frac{d\hat{m}}{dt} = -\gamma \hat{m} \times \vec{H}_{\text{eff}} + \alpha \hat{m} \times \frac{d\hat{m}}{dt} + a_J \hat{m} \times (\hat{m} \times \hat{m}_p) + b_J (\hat{m} \times \hat{m}_p) \quad (2)$$

where  $\hat{m} = M/M_s$  is the unit magnetization vector of the FL and  $M_s$  is the saturation magnetization.  $\hat{m}_p$  is the unit magnetization vector of the spin polarizer (i.e., RL).  $\gamma$  is the gyromagnetic constant and  $\alpha$  is the Gilbert damping factor.  $a_J$  and  $b_J$  are the torque factors of Slonczewski STT [3] and field-like STT [46]. In order to enable a quantitative comparison with the experimental results, we

have chosen parameters as close as possible to the experimental samples:  $M_s = 1000$  emu/cm<sup>3</sup> (saturation magnetization),  $A = 2 \times 10^{-11}$  J/m (exchange constant),  $K_u = 3 \times 10^4$  erg/cm<sup>3</sup> (magnetic anisotropy),  $\alpha = 0.01$  (damping constant),  $P = 0.56$  (spin polarization). The magnetization of RL is assumed to be fixed along the  $-x$  direction, and FL starts from a magnetization saturation state along the  $+x$  direction. In this simulation, the mesh cell of  $1 \times 1 \times 2$  nm<sup>3</sup> is used. The in-plane magnetic field  $H_{\parallel} = 2000$  Oe. The effective MW current density is estimated to be  $J_{\text{MW}} = 2.0 \times 10^7$  A/cm<sup>2</sup> based on our calibration of the MW transmission and nominal MW power applied. The frequency of the MW current-driving source ( $f_{\text{MW}}$ ) is changed from 5 to 20 GHz. The simulations at each driving frequency are taken over 20 ns to launch a stable magnetization precession and to obtain sufficient frequency resolution (smaller than 0.1 GHz). In our simulations, the MW current-induced Oersted field ( $H_{\text{Oe}}$ ) is neglected, as explained in detail in S-II within the Supplemental Material [34,47–49]. Previous studies have reported that in the nanocontact STT devices, the dc-current-induced  $H_{\text{Oe}}$  may modify the local energy landscape and generate multimodes in the FMR spectra [47], or increase the nucleation current of the droplet mode [48]. But, we note that the typical current density in the nanocontact devices is  $\sim 10^8$  A/cm<sup>2</sup>, i.e., one order higher than our case ( $2 \times 10^7$  A/cm<sup>2</sup>). As shown in Supplementary Fig. S2 [34], the calculated maximum amplitude of  $H_{\text{Oe}}$  is around 69 Oe at the outer side of the ring, which is still one order smaller than that of the nanocontact case. On the other hand, the  $H_{\text{Oe}}$  in our sample is caused by the ac current with GHz frequency, which means that the  $H_{\text{Oe}}$  is inhomogeneous both timewise and spatially. The effect of  $H_{\text{Oe}}$  would be averaged in the NR MTJs in one period ( $\sim 0.1$  ns for  $f_{\text{MW}} = 10$  GHz). As a result, the ac-current-induced Oersted field in our case can be neglected.

Figures 4(a)–4(f) show the spatially averaged magnetization over the whole FL of the NR MTJs  $\langle m_x \rangle$  response to the driving current source at a different frequency of  $f_{\text{MW}}$ . The precession is forced to launch as long as the MW current is injected, even though sometimes the oscillation amplitude is quite small. One can see that, when  $f_{\text{MW}}$  is much lower from  $f_{r1}$ , the precession amplitude is also very small ( $(\delta \langle m_x \rangle) \leq 0.02$ ), as shown in Figs. 4(a) and 4(b), suggesting that the magnetization of FL is only slightly driven away from its equilibrium position. As  $f_{\text{MW}}$  is increasing and approaching  $f_{r1}$ , the magnetization precession is also enhanced. An intensive precession with a relatively large amplitude ( $(\delta \langle m_x \rangle) \geq 0.15$ ) is then excited when  $f_{\text{MW}}$  is taken as 13.2 GHz, which corresponds to the first FMR state (mode 1), as depicted in Fig. 4(c). After that, the magnetization precession is suppressed again (Fig. 4(d),  $(\delta \langle m_x \rangle) \leq 0.02$ ). But with further increasing of  $f_{\text{MW}}$  close to  $f_{r2}$  of 17.4 GHz, the second resonance state (mode 2) is observed [Fig. 4(e)], at which the precession

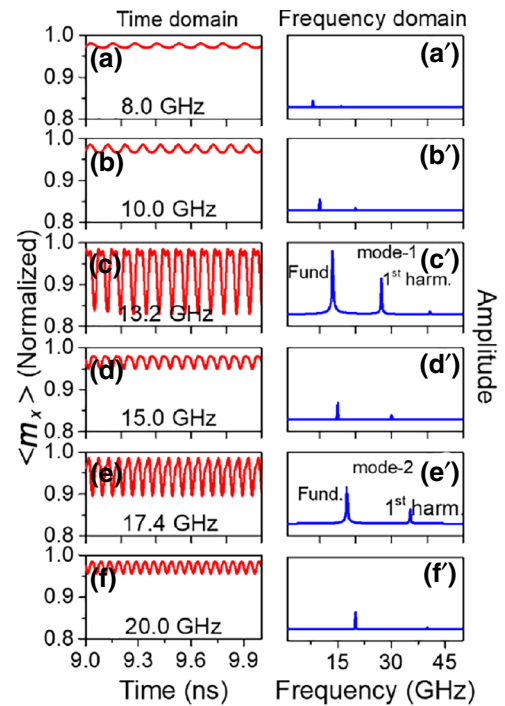


FIG. 4. (a)–(f) Spatially averaged magnetization  $\langle m_x \rangle$  precession driven by MW current at different frequencies. Two times of resonance states are clearly shown in (c),(e). (a')–(f') The corresponding frequency spectra calculated by FFT.

amplitude reaches an extremum ( $(\delta \langle m_x \rangle) = 0.1$ ) again. For  $f_{\text{MW}}$  higher than  $f_{r2}$ , no more resonance state is found in our simulated MW driving-frequency range ( $f_{\text{MW}} \leq 20$  GHz).

The time-dependent magnetization evolution in real space for the two resonance modes is also simulated and is shown in the Supplemental Video 1 [34], which can provide a clearer sight into the resonance states. We especially choose two typical regions A and B. We find that for mode 1, all the local magnetization almost precesses simultaneously in the same direction, including in part A and part B. While for mode 2, the local magnetizations in parts A and B precess in opposite directions. Accordingly, the phase evolution for  $m_y$  is discussed in Figs. 5(a) and 5(b), because the amplitude of magnetization precession in the movie is larger in the  $y$  direction. In mode 1, there are no obvious phase differences between points A and B, showing a synchronous in-phase precession. On the contrary, points A and B show antiphase states—a difference of  $180^\circ$ . This can be analogous with the movement of the lattices in the three-dimensional elementary cell, where the synchronous vibration of the lattices is regarded as an acoustic branch while the gravity center remains unperturbed during the complementary lattice vibration and is considered to be an optic branch [50]. As a result, mode 1 and mode 2 can be considered as acoustic-like and optic-like modes, respectively. This feature is very similar to the acoustic or optic mode observed in the coupled

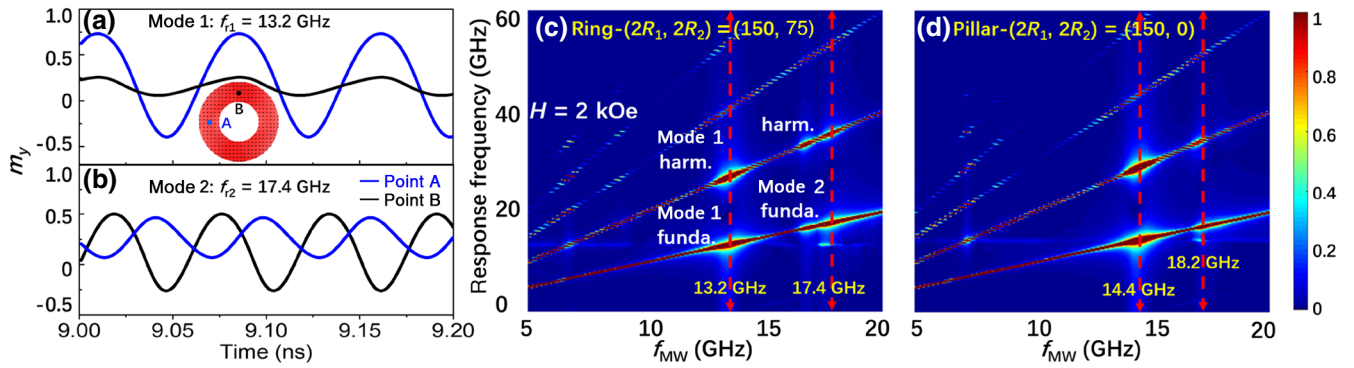


FIG. 5. Different types of local magnetization ( $m_y$ ) precessions taken at point A (blue curve) and point B (black curve) in the nanoring sample: (a) In-phase precession for the acoustic-like mode 1; (b) Antiphase precession for the optic-like mode 2. The mappings of the resonance signal as a function of the injected MW frequency are shown in (c) for NR MTJs and (d) for NP MTJs. Here, the outer diameter of the two samples is fixed to 150 nm and  $H_{\parallel} = 2$  kOe.

bilayer system [25–28], but the difference is that in our NR MTJs, both modes originate from the FL.

The simulation reproduces the experimental results well, showing that two different resonances can be excited by the ST FMR technique in the NR MTJs under a given  $H_{\parallel}$ . And since the two resonances are independent and can be separately excited, we recognize these two resonance states as fundamental resonances. Interestingly, in addition to the large amplitude of the magnetization oscillation shown in the time domain, it is also noteworthy in Figs. 4(c) and 4(e) that a noticeable small ripple of magnetization oscillation is superimposed over the resonance curves. This means that in addition to the two fundamental ones, additional precessions with frequencies differing from  $f_{r1}$  and  $f_{r2}$  are also simultaneously excited at a fixed driving frequency  $f_{MW}$ . However, the amplitudes of these additional oscillations are very small, therefore, we consider them to be secondary precessions (high-order harmonics), corresponding to the fundamental ones.

The above spin-torque-driven resonance features can be seen more straightforwardly by translating the time-domain simulations into frequency-domain simulations with the FFT technique. The frequency spectrum is calculated from  $\langle m_x \rangle$ , as shown in Figs. 4(a')–(f'). Consistent with the magnetization precession amplitude, the peak of the frequency spectra also reach the extremum value when the resonance condition  $f_{MW} = f_{r1}$  or  $f_{r2}$  is satisfied; otherwise, the precession amplitude always remains low. In addition to the fundamental resonances of mode 1 and mode 2, it is also clearly seen that the first-order harmonics (1st harm.) with a frequency twice that of  $f_{r1}$  and  $f_{r2}$  is shown in the frequency spectra (26.4 GHz and 34.8 GHz), see Figs. 4(c') and 4(e'), respectively. These high-order harmonics may correspond to the small ripples of  $\langle m_x \rangle$  curves shown in Figs. 4(c) and 4(e).

The detailed ST FMR response frequency signal as a function of the driving frequency  $f_{MW}$  for the NR MTJs

is summarized in Fig. 5(c), in which the applied magnetic field  $H_{\parallel}$  is fixed at 2000 Oe. Generally speaking, the first-order harmonic precession is accompanied by even higher order harmonics [6]. This is confirmed by Fig. 5(c), showing the occurrence of the two fundamental modes and first-order harmonics, as well as the even higher-order harmonics modes. We find that these resonance states can also be observed in the circular geometric confined NP MTJs, as shown in Fig. 5(d). The difference is that the frequency of mode 1 is shifted to 14.4 GHz, while that of mode 2 is shifted to 18.2 GHz. We also simulated a series of NR MTJs with different inner diameters ( $2R_2 = 0, 50, 75, 120$ , in nanometers), as shown in S-III within the Supplemental Material [34], in which the outer diameter  $2R_1$  is fixed to 150 nm. As the inner diameter increases (i.e. ring width decreasing) from 0 to 120 nm,  $f_{r1}$  decreases from 14.4 to 12.5 GHz, showing a redshift. But for the very thin NR MTJ case as shown in Fig. S3(f) within the Supplemental Material [34], an intermixed resonance mode appears in the response of the resonances, which could be the result of the increase of demagnetization energy of system since the magnetic onion state could fall into a nonuniform state with the shrinking of the ring width. This is evidence of the geometrically confined effect.

Generally, the peaks in the frequency domain of Fig. 4 represent different kinds of oscillation modes, which can be analyzed individually. This can be done by means of windowed Fourier transform, described in detail in Ref. [51–53]. First, the oscillations of magnetization at each mesh cell are transformed into the frequency domain. Then, a small frequency range at the objective mode is selected and the oscillations with the frequencies within this range are transformed back to the time domain. In this way, the spatiotemporal evolution of local magnetization oscillations  $\delta m_x$  which contributes to the selected frequency mode can be reconstructed by using the amplitude and the phase of local magnetization oscillations.

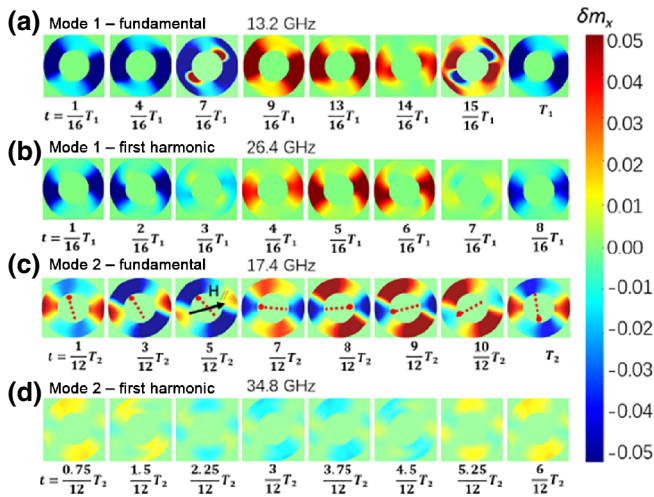


FIG. 6. Snapshot evolutions of the reconstructive magnetization component  $\delta m_x$  for the (a) mode 1, (b) first-order harmonic of mode 1, (c) mode 2 and (d) first-order harmonic of mode 2. The dashed red ray in (c) is for view guiding to show the rotation of the quadrant structure.

Thus, the parts of the domains as well as the details of precession under the special frequency can be clearly recognized. Figures 6(a)–6(d) show the reconstructed oscillation mode profiles from the Fourier filtering at the different modes or harmonics with their respective frequencies, in which the model structures in  $\delta m_x$  evolution in one period ( $T$ ) are presented. All these snapshots are taken from the videos in Supplemental Videos 2–5 [34], in which the motion of  $\delta m_x$  is much more intuitive and obvious. For example, for the fundamental resonance mode 1 shown in Fig. 6(a) (snapshots taken from movie M2), the period  $T_1 = 1/f_{r1}$ , which records from an initial state with  $\delta m_x$  aligned to the  $-x$  direction ( $\delta m_x < 0$ ) and magnetization domain is divided into two blue half-rings ( $1T_1/16$ ) due to the different oscillation amplitudes. Then,  $\delta m_x$  is gradually transformed into a quadrant structure ( $7T_1/16$ ), in which the two red parts of  $\delta m_x$  are distributed along the positive direction ( $\delta m_x > 0$ ) while the other blue parts are distributed along the negative ( $\delta m_x < 0$ ) direction. After that, the red area of the positive  $\delta m_x$  is further enlarged and erodes the quadrant state until two new positive  $\delta m_x$  half-ring states are established ( $9T_1/16$ ). In the next half period,  $\delta m_x$  is then transformed back to the same negative direction state as the initial one, also with a quadrant state at  $15T_1/16$  during the evolution. The periodical evolution of magnetization precession in this modal structure contributes to fundamental resonance mode 1 with a frequency of  $f_{r1}$ , which equals 13.2 GHz.

In contrast, for the fundamental resonance mode 2, which has a higher resonance frequency  $f_{r2}$  of 17.4 GHz, the simulation reveals that it has different modal structures with increased azimuthal nodal lines and a different rotational mode. This can be seen from the supplementary

Movie 4 [34] and the corresponding snapshots shown in Fig. 6(c), in which,  $\delta m_x$  of the FL retains an asymmetry quadrant structure for the whole period ( $T_2 = 1/f_{r2}$ ). Four separated regions with  $\delta m_x > 0$  and  $\delta m_x < 0$  alternately show up in the ring, forming a quadrant structure. Actually, different from the circumstance in mode 1 mentioned above, the four regions are driven into rotation in a counterclockwise direction, shown by the dashed red rays. The negative blue parts start to enlarge from  $1T_1/12$ , until  $5T_1/12$  to the extreme amplitude. Then they tend to be eroded by the positive red parts and shrink to a minimum until  $10T_1/12$ . In addition, the two states located along the  $H_{\parallel}$  direction are always smaller than the other two, which are vertical to  $H_{\parallel}$ , which may be due to the constraint effect of  $H_{\parallel}$ .

A similar analysis is also conducted on the first-order harmonic resonances, as shown in Fig. 6(b) and 6(d). It is found that the magnetization dynamic structures and the time-evolution features of the harmonic resonances are similar to those of the corresponding fundamental modes, except that the time period is half that of the fundamental modes. Unfortunately, however, these high-order harmonics can not be observed in our experiments due to the small oscillation signal and limited detecting frequency of the instruments. Details of the evolution of  $\delta m_x$  for the first-order harmonics resonance of mode 1 and mode 2 can be found in the Supplemental Video 3 and Video 5 [34], respectively.

Finally, an analytical theory based on a standing spin wave (SSW) is developed to explain the acoustic-like mode 1 and optic-like mode 2. From the basic FMR principles [27,28,54,55], the resonance frequency can be written as follows:

$$\omega = \frac{\gamma}{M_s \sin \theta} \sqrt{\frac{\partial^2 F}{\partial \theta^2} \frac{\partial^2 F}{\partial \varphi^2} - \left( \frac{\partial^2 F}{\partial \theta \partial \varphi} \right)^2} \quad (3)$$

where  $\gamma$  ( $= 1.76 \times 10^{11} \text{ s}^{-1} \text{ T}^{-1}$ ) is the gyromagnetic ratio and  $\theta$  and  $\varphi$  are the angles in spherical coordinates corresponding to the magnetization vector  $\mathbf{M}$ .  $F$  is the system free-energy density. Considering that the samples presented in this study are geometrically confined, the spin wave could be excited. In our case, the 2 nm-thick FL cannot possibly support the SSW propagating in the perpendicular direction. But the spin waves can travel through the in-plane film to the (inner or outer) side surfaces of rings, at which they are reflected and return back to the FL, forming the SSWs. Due to the nonuniform oscillation in the SSW modes, the frequency should depend on the exchange interaction. Therefore,  $F$  reads

$$F = -K_u \sin^2 \theta \cos^2 \varphi - \mu_0 M_s H_{\parallel} \sin \theta \cos \varphi + \frac{1}{2} \mu_0 M_s^2 \cos^2 \theta$$

$$+ \frac{A}{M_s^2} [(\nabla m_x)^2 + (\nabla m_y)^2 + (\nabla m_z)^2] \quad (4)$$

The four terms in Eq. (4) stand for the uniaxial anisotropy energy, Zeeman energy, demagnetization energy, and exchange energy ( $F_{\text{exc}}$ ), respectively. Here,  $A$  is the exchange constant with a value of  $2 \times 10^{-11}$  J/m. Considering the effect of exchange interaction, the magnetization can be described as a plane wave with the form of  $e^{-(\omega t - \mathbf{k} \cdot \mathbf{r})}$  at position  $\mathbf{r}$  with the wavevector  $\mathbf{k}$  in a resonance state, supposing that the magnetization oscillates in the  $xOy$  plane, with  $H_{\parallel}$  along the  $x$  direction. The sample boundary condition determines the value of the  $\mathbf{k}$  vector for the node order of the SSW [56]:

$$k = \frac{n\pi}{d} \quad (n = 0, 1, 2, \dots) \quad (5)$$

where  $d$  represents the size of the MTJs. In our case, the magnetization forms an onion state in the ring under  $H_{\parallel}$ , which is along the  $-x$  direction, resulting in  $M_x \approx M_s$  and  $F_{\text{exc}}$  is reduced to [57]:

$$F_{\text{exc}} = \frac{A}{M_s^2} k^2 M_y^2 - k^2 A (m_y^2 + m_z^2) \quad (6)$$

Thus, the resonance frequency for the standing SW modes can be written as

$$f = \frac{\gamma}{2\pi} \sqrt{\left(\frac{2K_u}{M_s} + \mu_0 M_s + \mu_0 H_{\parallel} - \frac{2k^2 A}{M_s}\right)} \times \sqrt{\left(\frac{2K_u}{M_s} + \mu_0 H_{\parallel} - \frac{2k^2 A}{M_s}\right)} \quad (7)$$

For the NP MTJs, the diameter  $2R_1 = 150$  nm and the SSW node  $n = 1$ . Taking other parameters as mentioned in the main text for the CoFeB free layer, we get  $\mu_0 H_k = 2K_u/M_s \sim 0.006$  T,  $\mu_0 M_s = 1.25$  T,  $\mu_0 H_{\parallel} = 0.2$  T, and  $2k^2 A/M_s = 0.0175$  T. By taking  $A$  as a positive value ( $2 \times 10^{-11}$  J/m) for the in-phase precession mode 1 [Fig. 5(a)],  $f_{r1}$  is obtained as 14.3 GHz. For mode 2, since there are antiphase precession regions,  $A$  should be taken as a negative value of  $-2 \times 10^{-11}$  J/m and we get  $f_{r2} = 16.1$  GHz. These theoretical values are consistent with those shown in Fig. 5(d).

For the NR MTJs, we notice that the existence of an inner side surface will decrease the effective area for propagating spin waves. Without loss of generality, we introduce a confinement factor  $\sigma$  for this change, which could influence the exchange interaction contribution, as

$$F_{\text{exc}}^{\text{NR MTJ}} = \sigma F_{\text{exc}}^{\text{NP MTJ}} \quad (8)$$

Thus, by adding  $\sigma = 2.5$  for the NR MTJs with  $(2R_1, 2R_2) = (150, 75)$ , we get  $f_{r1} = 13.3$  GHz and  $f_{r2} = 17.4$  GHz,

respectively, in which the exchange constants  $A$  are taken as positive and negative values for mode 1 and mode 2, respectively. These are perfectly consistent with the simulated values shown in Fig. 5(a), evidencing the shape-confinement effect of the MTJs on the ST FMR spectra.

If we consider the homogeneously precessing magnetization within the entire sample, in which case all the spins rotate coherently, the system can be treated as a macrospin model. Then, the exchange interaction effect is neglected ( $A = 0$ ). By evaluating the realistic in-plane precession case with  $\theta = \pi/2$ , Eq. (7) is reduced to the Kittel formula as shown in Eq. (9), which makes the SSW-based theoretical analysis coherent.

$$\omega = \gamma \sqrt{\left(\frac{2K_u}{M_s} + \mu_0 M_s + \mu_0 H_{\parallel}\right) \left(\frac{2K_u}{M_s} + \mu_0 H_{\parallel}\right)} \quad (9)$$

Thus, we reach the conclusion that the experimentally and theoretically observed dual-mode ST FMR signal comes from the exchange-dominated spin waves together with the shape confinement effect.

Based on the observation of the acoustic-like and optic-like modes in the same NR MTJ device under one fixed magnetic field, the MW detector can be extended to a double-detecting mode—two different frequencies can launch the resonance states in the NR MTJs and both can be detected. Additionally, with the observation of the harmonic resonance modes, it is itself a strong confirmation of the detecting results, which means the sensitivity of the dual-mode detector can be improved.

#### IV. SUMMARY

In summary, by launching the ST FMR measurement in the ring-shape confined NR MTJs, two resonance states are observed under a given external magnetic field, which can be driven independently and separately. These two resonance modes correspond to the acoustic-like resonance mode 1 and optic-like resonance mode 2, respectively, which is supported by our simulations and analytical theory. Higher-order harmonic resonances are also observed for each fundamental one. Additionally, for all the resonances, the magnetization domain is driven into a rotation state, which is a direct result of the spinwave propagation and NR-confined effect. Based on these results, a dual-mode MW detector with higher sensitivity is proposed.

#### ACKNOWLEDGMENTS

This work was supported by the National Key Research and Development Program of China (MOST, Grants No. 2017YFA0206200), the National Natural Science Foundation of China (NSFC, Grants No. 11434014, No. 51620105004, and No. 11674373), and partially supported by the Strategic Priority Research Program (B)

(Grant No. XDB07030200), the International Partnership Program (Grant No. 112111KYBS20170090), and the Key Research Program of Frontier Sciences (Grant No. QYZDJ-SSWSLH016) of the Chinese Academy of Sciences (CAS).

- 
- [1] S. A. Wolf, D. D. Awschalom, R. A. Buhrman, J. M. Daughton, S. Von Molnar, M. L. Roukes, A. Yu. Chtchelkanova, and D. M. Treger, Spintronics: A spin-based electronics vision for the future, *Science* **294**, 1488 (2001).
- [2] Zhongming Zeng, Pedram Khalili Amiri, Ilya N. Krivorotov, Hui Zhao, Giovanni Finocchio, Jian-Ping Wang, Jordan A. Katine, Yiming Huai, Juergen Langer, and Kosmas Galatsis *et al.*, High-power coherent microwave emission from magnetic tunnel junction nano-oscillators with perpendicular anisotropy, *ACS Nano* **6**, 6115 (2012).
- [3] John C. Slonczewski, Current-driven excitation of magnetic multilayers, *J. Magn. Mater.* **159**, L1 (1996).
- [4] H.-S. Philip Wong and Sayeef Salahuddin, Memory leads the way to better computing, *Nat. Nanotechnol.* **10**, 191 (2015).
- [5] Zhitao Diao, Zhanjie Li, Shengyuang Wang, Yunfei Ding, Alex Panchula, Eugene Chen, Lien-Chang Wang, and Yiming Huai, Spin-transfer torque switching in magnetic tunnel junctions and spin-transfer torque random access memory, *J. Phys.: Condens. Matter* **19**, 165209 (2007).
- [6] Jack C. Sankey, Yong-Tao Cui, Jonathan Z. Sun, John C. Slonczewski, Robert A. Buhrman, and Daniel C. Ralph, Measurement of the spin-transfer-torque vector in magnetic tunnel junctions, *Nat. Phys.* **4**, 67 (2008).
- [7] S. Y. Martin, N. De Mestier, C. Thirion, Christophe Hoarau, Yann Conraux, Claire Baraduc, and Bernard Diény, Parametric oscillator based on nonlinear vortex dynamics in low-resistance magnetic tunnel junctions, *Phys. Rev. B* **84**, 144434 (2011).
- [8] Burkard Hillebrands and Kamel Ounadjela, *Spin Dynamics in Confined Magnetic Structures I* (Springer Science & Business Media, Berlin, 2003), Vol. 83.
- [9] Jian Zhu, J. A. Katine, Graham E. Rowlands, Yu-Jin Chen, Zheng Duan, Juan G. Alzate, Pramey Upadhyaya, Juergen Langer, Pedram Khalili Amiri, and Kang L. Wang *et al.*, Voltage-induced ferromagnetic resonance in magnetic tunnel junctions, *Phys. Rev. Lett.* **108**, 197203 (2012).
- [10] Bretislav Heinrich, S. T. Purcell, J. R. Dutcher, K. B. Urquhart, J. F. Cochran, and A. S. Arrott, Structural and magnetic properties of ultrathin ni/fe bilayers grown epitaxially on ag (001), *Phys. Rev. B* **38**, 12879 (1988).
- [11] G. Finocchio, I. N. Krivorotov, X. Cheng, L. Torres, and B. Azzaroni, Micromagnetic understanding of stochastic resonance driven by spin-transfer-torque, *Phys. Rev. B* **83**, 134402 (2011).
- [12] Daniel C. Ralph and Mark D. Stiles, Spin transfer torques, *J. Magn. Mater.* **320**, 1190 (2008).
- [13] Eric R. Everts, Matthew R. Pufall, and William H. Rippard, Continuous-film vs. device-level ferromagnetic resonance in magnetic tunnel junction thin films, *J. Appl. Phys.* **113**, 083903 (2013).
- [14] C. Wang, Y.-T. Cui, J. Z. Sun, J. A. Katine, R. A. Buhrman, and D. C. Ralph, Bias and angular dependence of spin-transfer torque in magnetic tunnel junctions, *Phys. Rev. B* **79**, 224416 (2009).
- [15] J. C. Sankey, P. M. Braganca, A. G. F. Garcia, I. N. Krivorotov, R. A. Buhrman, and D. C. Ralph, Spin-transfer-driven ferromagnetic resonance of individual nanomagnets, *Phys. Rev. Lett.* **96**, 227601 (2006).
- [16] Hamid Mazraati, Tuan Q. Le, Ahmad A. Awad, Sunjae Chung, Eriko Hirayama, Shoji Ikeda, Fumihiko Matsukura, Hideo Ohno, and Johan Åkerman, Free-and reference-layer magnetization modes versus in-plane magnetic field in a magnetic tunnel junction with perpendicular magnetic easy axis, *Phys. Rev. B* **94**, 104428 (2016).
- [17] G. N. Kakazei, P. E. Wigen, K. Yu. Guslienko, V. Novosad, A. N. Slavin, V. O. Golub, N. A. Lesnik, and Y. Otani, Spin-wave spectra of perpendicularly magnetized circular submicron dot arrays, *Appl. Phys. Lett.* **85**, 443 (2004).
- [18] Robert D. McMichael and Mark D. Stiles, Magnetic normal modes of nanoelements, *J. Appl. Phys.* **97**, 10J901 (2005).
- [19] Hong-Xiang Wei, Mark C. Hickey, Graham I. R. Anderson, Xiu-Feng Han, and Christopher H. Marrows, Current-induced magnetization switching in a microscale ring-shaped magnetic tunnel junction, *Phys. Rev. B* **77**, 132401 (2008).
- [20] X. F. Han, Z. C. Wen, Y. Wang, L. Wang, and H. X. Wei, Nano-scale patterned magnetic tunnel junction and its device applications, *AAPPS Bull.* **18**, 25 (2008).
- [21] Hong-Xiang Wei, Jiexuan He, Zhen-Chao Wen, Xiu-Feng Han, Wen-Shan Zhan, and Shufeng Zhang, Effects of current on nanoscale ring-shaped magnetic tunnel junctions, *Phys. Rev. B* **77**, 134432 (2008).
- [22] Zheng Li, Xiuyuan Bi, Hai Helen Li, Yiran Chen, Jianying Qin, Peng Guo, Wenjie Kong, Wenshan Zhan, Xiufeng Han, and Hong Zhang *et al.*, in *Proceedings of the 2016 International Symposium on Low Power Electronics and Design* (ACM, San Francisco, 2016), p. 4–9.
- [23] X. F. Han, Z. C. Wen, Y. Wang, H. F. Liu, H. X. Wei, and D. P. Liu, Nanoelliptic ring-shaped magnetic tunnel junction and its application in mram design with spin-polarized current switching, *IEEE Trans. Magn.* **47**, 2957 (2011).
- [24] X. F. Han, Z. C. Wen, and H. X. Wei, Nanoring magnetic tunnel junction and its application in magnetic random access memory devices with spin-polarized current switching, *J. Appl. Phys.* **103**, 07E933 (2008).
- [25] C. Berk, F. Ganss, M. Jaris, M. Albrecht, and H. Schmidt, All-optical measurement of interlayer exchange coupling in Fe/Pt/FePt thin films, *Appl. Phys. Lett.* **112**, 052401 (2018).
- [26] Zhen Li, Ralph Skomski, Sy-Hwang Liou, Steven Michalski, Mircea Chipara, and Roger D. Kirby, Magnetization precession and domain-wall structure in cobalt-ruthenium-cobalt trilayers, *J. Appl. Phys.* **109**, 07C113 (2011).
- [27] J Lindner and K Baberschke, Ferromagnetic resonance in coupled ultrathin films, *J. Phys.: Condens. Matter* **15**, S465 (2003).
- [28] Yunpeng Chen, Xin Fan, Yang Zhou, Yunsong Xie, Jun Wu, Tao Wang, Siu Tat Chui, and John Q. Xiao, Designing and tuning magnetic resonance with exchange interaction, *Adv. Mater.* **27**, 1351 (2015).



- [29] Xin Fan, Rong Cao, Takahiro Moriyama, Weigang Wang, H. W. Zhang, and John Q. Xiao, Magnetic tunnel junction based microwave detector, *Appl. Phys. Lett.* **95**, 122501 (2009).
- [30] L. Fu, Z. X. Cao, S. Hemour, K. Wu, D. Houssameddine, W. Lu, S. Pistorius, Y. S. Gui, and C.-M. Hu, Microwave reflection imaging using a magnetic tunnel junction based spintronic microwave sensor, *Appl. Phys. Lett.* **101**, 232406 (2012).
- [31] C. Wang, Y.-T. Cui, J. Z. Sun, J. A. Katine, R. A. Buhrman, and D. C. Ralph, Sensitivity of spin-torque diodes for frequency-tunable resonant microwave detection, *J. Appl. Phys.* **106**, 053905 (2009).
- [32] Charles Kittel, On the theory of ferromagnetic resonance absorption, *Phys. Rev.* **73**, 155 (1948).
- [33] Charles Kittel, Paul McEuen, and Paul McEuen, *Introduction to Solid State Physics* (Wiley, New York, 1996), Vol. 8.
- [34] See Supplemental Material (docx and movies) at <http://link.aps.org/supplemental/10.1103/PhysRevApplied.0.XXXX> XX for: S-I, the impact of stray field on FMR spectra; S-II, the impact of Oersted field on FMR spectra; S-III, FMR responses for MTJs with different size parameters; Video 1, magnetization resonance dynamics of acoustic-like and optic-like modes in real space; Videos 2 and 3, domain motion for acoustic-like mode in fundamental and first harmonic resonance states, respectively; Videos 4 and 5, domain motion for optic-like mode in fundamental and first harmonic resonance states, respectively.
- [35] Jiang Xiao, A. Zangwill, and Mark D. Stiles, Macrospin models of spin transfer dynamics, *Phys. Rev. B* **72**, 014446 (2005).
- [36] S. Petit, C. Baraduc, C. Thirion, U. Ebels, Y. Liu, Mo Li, P. Wang, and B. Dieny, Spin-torque influence on the high-frequency magnetization fluctuations in magnetic tunnel junctions, *Phys. Rev. Lett.* **98**, 077203 (2007).
- [37] S. Petit, N. De Mestier, Claire Baraduc, C. Thirion, Y. Liu, M. Li, P. Wang, and B. Dieny, Influence of spin-transfer torque on thermally activated ferromagnetic resonance excitations in magnetic tunnel junctions, *Phys. Rev. B* **78**, 184420 (2008).
- [38] Nils Kuhlmann, Andreas Vogel, and Guido Meier, Magnetization dynamics and cone angle precession in permalloy rectangles, *Phys. Rev. B* **85**, 014410 (2012).
- [39] Th Gerrits, Michael L. Schneider, Anthony B. Kos, and Thomas J. Silva, Large-angle magnetization dynamics measured by time-resolved ferromagnetic resonance, *Phys. Rev. B* **73**, 094454 (2006).
- [40] Luc Thomas, Guenole Jan, Son Le, Santiago Serrano-Guisan, Yuan-Jen Lee, Huanlong Liu, Jian Zhu, Jodi Iwata-Harms, Ru-Ying Tong, and Sahil Patel *et al.*, in *2017 IEEE International Electron Devices Meeting (IEDM)* (IEEE, San Francisco, 2017) p. 38.
- [41] Michael Farle, Tom Silva, and Georg Woltersdorf, in *Magnetic Nanostructures* (Springer, Berlin, 2013), p. 37.
- [42] C. T. Boone, J. A. Katine, J. R. Childress, Vasil Tiberkevich, Andrei Slavin, Jian Zhu, Xiao Cheng, and I. N. Krivorotov, Resonant nonlinear damping of quantized spin waves in ferromagnetic nanowires: A spin torque ferromagnetic resonance study, *Phys. Rev. Lett.* **103**, 167601 (2009).
- [43] Hans T. Nembach, Justin M. Shaw, Carl T. Boone, and Thomas J. Silva, Mode-and size-dependent Landau-Lifshitz damping in magnetic nanostructures: Evidence for nonlocal damping, *Phys. Rev. Lett.* **110**, 117201 (2013).
- [44] W. Chen, G. De Loubens, J.-M. L. Beaujour, A. D. Kent, and J. Z. Sun, Finite size effects on spin-torque driven ferromagnetic resonance in spin valves with a Co/Ni synthetic free layer, *J. Appl. Phys.* **103**, 07A502 (2008).
- [45] The object oriented micromagnetic framework (oommf) project at itl/nist, <https://math.nist.gov/oommf/>.
- [46] Z. Li, S. Zhang, Z. Diao, Y. Ding, X. Tang, D. M. Apalkov, Z. Yang, K. Kawabata, and Y. Huai, Perpendicular spin torques in magnetic tunnel junctions, *Phys. Rev. Lett.* **100**, 246602 (2008).
- [47] Randy K. Dumas, Ezio Iacocca, Stefano Bonetti, S. R. Sani, Seyed Majid Mohseni, Anders Eklund, Johan Persson, Olle Heinonen, and Johan Åkerman, Spin-wave-mode coexistence on the nanoscale: A consequence of the Oersted-field-induced asymmetric energy landscape, *Phys. Rev. Lett.* **110**, 257202 (2013).
- [48] Sheng Jiang, Seyyed Ruhollah Etesami, Sunjae Chung, Quang Tuan Le, Afshin Houshang, and Johan Åkerman, Impact of the Oersted field on droplet nucleation boundaries, *IEEE Magn. Lett.* **9**, 1 (2018).
- [49] G. Consolo, B. Azzarboni, G. Finocchio, L. Lopez-Diaz, and L. Torres, Influence of the Oersted field in the dynamics of spin-transfer microwave oscillators, *J. Appl. Phys.* **101**, 09C108 (2007).
- [50] B. N. Brockhouse, Lattice vibrations in silicon and germanium, *Phys. Rev. Lett.* **2**, 256 (1959).
- [51] Marcos Grimsditch, Gary K. Leaf, Hans G. Kaper, Dmitry A. Karpeev, and Robert E. Camley, Normal modes of spin excitations in magnetic nanoparticles, *Phys. Rev. B* **69**, 174428 (2004).
- [52] Ming Yan, Riccardo Hertel, and Claus M. Schneider, Calculations of three-dimensional magnetic normal modes in mesoscopic permalloy prisms with vortex structure, *Phys. Rev. B* **76**, 094407 (2007).
- [53] Hong Zhang, Yaowen Liu, Ming Yan, and Riccardo Hertel, Azimuthal spin wave modes excited in an elliptical nanomagnet with vortex pair states, *IEEE Trans. Magn.* **46**, 1675 (2010).
- [54] J. Smith and H. G. Beljers, Ferromagnetic resonance absorption in BaFe<sub>12</sub>O<sub>19</sub>, a highly anisotropic crystal, *Phillips Res. Rep.* **10**, 113 (1955).
- [55] Sergey O. Demokritov, Burkard Hillebrands, and Andrei N. Slavin, Confined dynamic excitations in structured magnetic media, *IEEE Trans. Magn.* **38**, 2502 (2002).
- [56] A. G. Gurevich and G. A. Melkov, *Magnetization Oscillations and Waves* (CRC Press, New York, 1996), p. 245.
- [57] Marija Djordjevic Kaufmann, *Magnetization Dynamics in All-Optical Pump-Probe Experiments: Spin-Wave Modes and Spin-Current Damping* (University of Göttingen, Göttingen, 2006).